JGR Space Physics

RESEARCH ARTICLE
10.1029/2021JA029207

Special Section:
Geospace multi-point observations in Van Allen Probes and Arase era

# Embedded Regions 1 and 2 Field-Aligned Currents: Newly Recognized From Low-Altitude Spacecraft Observations

**Jiang Liu[1,2], L. R. Lyons[2], Chih-Ping Wang[2], Yuzhang Ma[3], R. J. Strangeway[1], Yongliang Zhang[4], M. Kivelson[1], Ying Zou[5], and K. Khurana[1]**

[1]Department of Earth, Planetary, and Space Sciences, University of California, Los Angeles, Los Angeles, CA, USA, [2]Department of Atmospheric and Oceanic Sciences, University of California, Los Angeles, Los Angeles, CA, USA, [3]Shandong University, Weihai, China, [4]Applied Physics Laboratory, Laurel, MD, USA, [5]Department of Space Science, University of Alabama, Huntsville, AL, USA

**Abstract** Regions 1 and 2 (R1 and R2) field-aligned currents (FACs), manifestations of large-scale convection in Earth's magnetosphere-ionosphere (M-I) system, often contain intense FAC layers of mesoscale latitudinal width near the R1/R2 interface. We refer to such layers as "embedded" R1 and R2 FACs. Likely resulting from enhanced magnetosphere-ionosphere (M-I) convection, these FACs may indicate M-I configuration change and contribute significantly to substorm current wedges. We present several events in which embedded FACs were observed by low-altitude spacecraft in the ionosphere. All the events occurred during active geomagnetic conditions or a substorm growth phase, and most map to an equatorial location on the nightside. When an embedded FAC is upward, it coincides with inverted-V electron precipitation and a discrete auroral arc. If an upward embedded FAC is in the postmidnight-to-dawn sector, a dawnside auroral polarization stream appears immediately poleward of it, so it may be important for ionospheric heating, M-I convection, and instabilities. Our results establish embedded FACs as a frequently appearing, fundamental phenomenon for understanding and modeling the magnetosphere-ionosphere system.

**Plain Language Summary** Earth's magnetosphere is coupled to its ionosphere by currents flowing along magnetic fields. We introduce and investigate one type of such currents observed by low-altitude spacecraft flying in the ionosphere. We found that these currents, which are related to bright aurora and strong plasma flows, likely result from and indicate active magnetotail conditions and may be important for understanding energy transport and conversion in the magnetosphere-ionosphere system.

**Key Points:**

- Embedded Regions 1 and 2 currents are intense, latitudinally mesoscale, field-aligned currents (FACs) adjacent to the region 1/2 interface
- Embedded FACs coincide with inverted-V precipitation, discrete auroral arcs, and fast ionospheric flows
- Embedded FACs may result from enhanced magnetosphere-ionosphere convection

**Correspondence to:**
J. Liu,
jliu@igpp.ucla.edu

**Citation:**
Liu, J., Lyons, L. R., Wang, C.-P., Ma, Y., Strangeway, R. J., Zhang, Y., et al. (2021). Embedded Regions 1 and 2 field-aligned currents: Newly recognized from low-altitude spacecraft observations. *Journal of Geophysical Research: Space Physics*, *126*, e2021JA029207. https://doi.org/10.1029/2021JA029207

Received 6 FEB 2021
Accepted 15 MAY 2021



## 1. Introduction

Earth's magnetosphere is electromagnetically coupled to its ionosphere by field-aligned currents (FACs) comprising two large-scale elements, Region 1 (R1) and Region 2 (R2) currents, which were discovered by Iijima and Potemra (1976a, 1976b) in the ionosphere (Figure 1a). Region 1 currents, which are at higher latitudes, consist of FACs flowing downward into the ionosphere in the dawn sector and upward out of the ionosphere in the dusk sector. Equatorward of R1 currents lie R2 currents, which flow in the opposite directions. Regions 1 and 2 currents largely overlap the auroral oval, the ionospheric footprint of the plasma sheet. In the magnetosphere (Figure 1b), R1 current occupies a large volume, including the magnetopause, the plasma sheet boundary layer, and the outer (high invariant latitude) plasma sheet. Region 2 current occupies the inner (lower invariant latitude) plasma sheet, including the central plasma sheet, and part of the inner magnetosphere (e.g., Cowley, 2000; Ohtani et al., 1988, 2010; Tanaka, 1995). The equatorial footprint of the interface between R1 and R2 currents is at ~8–12 $R_E$ downtail on the nightside (Liu et al., 2016). These currents, which arise from large-scale M-I convection and its resultant magnetic field distortions and pressure gradients (Tanaka, 1995), are critical to imposing magnetic stress, modifying plasma flow, and transmitting energy between the ionosphere and the magnetosphere (e.g., Vasyliunas, 1970).

Well-approximated as current sheets elongated in the east-west direction (Figure 1; in this paper, east, west, north, and south refer to magnetic east, west, north, and south, respectively), R1 and R2 currents cause deflection of the east-west magnetic field ($B_E$) in the ionosphere. Iijima and Potemra (1976a, 1976b) relied on the $B_E$ deflection profile as a function of magnetic latitude to discover R1 and R2 currents, and it remains a

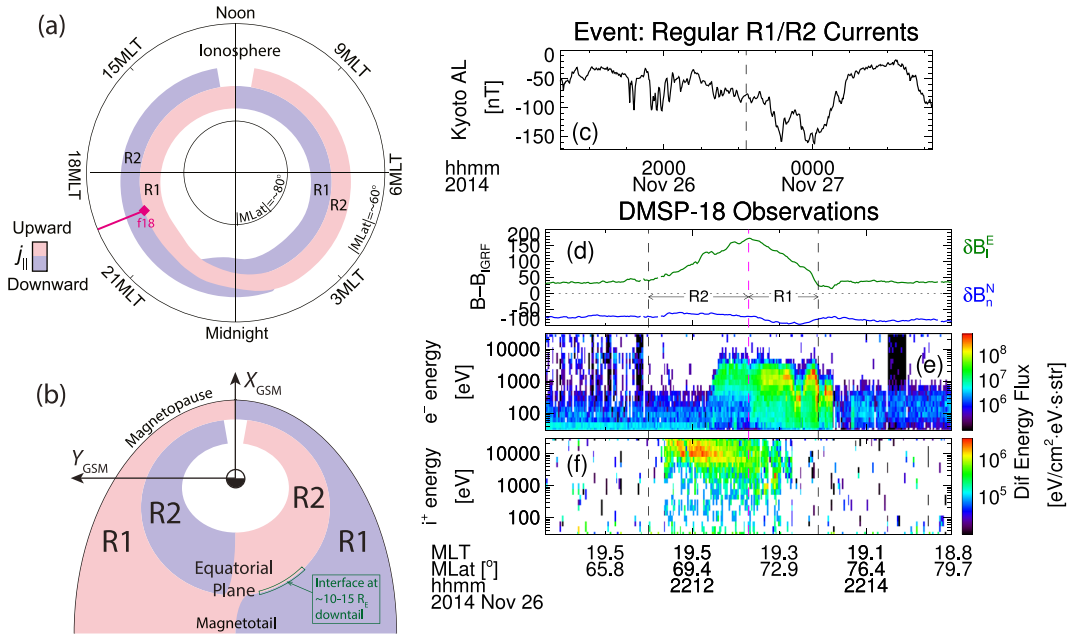


**Figure 1.** (a) Cartoon illustrating the locations of Regions 1 and 2 currents in the ionosphere. Light red/blue: upward/downward field-aligned currents. The magenta line and diamond: schematic track and location, respectively, of DMSP-18 giving the measurements in (d–f), at 2212:39UT, November 26, 2014. (b) R1 and R2 currents' equatorial footprints in the $XY_{GSM}$ plane. Note that the FACs vanish on this plane (or more precisely, on the neutral sheet) and grow away from it northward and southward along field lines. (c) Kyoto AL index. The vertical dashed line indicates 2212:39UT. (d) Components of the perturbation magnetic field vector after the IGRF has been subtracted. Vertical dashed lines indicate the boundaries of R1 and R2 currents; the magenta line marks their interface. Green/blue: maximum/minimum variance component of the horizontal field, approximately eastward/northward. (e and f) Differential energy flux of precipitating electrons/ions.

key indicator of their global distribution. This profile is best observed by a low-altitude (<1 $R_E$ from Earth's surface) spacecraft moving in the north-south direction. Figure 1d shows such an observation of typical R1 and R2 currents during relatively quiet conditions (AL ~−70 nT; Figure 1c) by a DMSP (Defense Meteorological Satellite Program) spacecraft at ~840 km altitude traveling from south to north in the northern hemisphere (see trajectory in Figure 1a). The eastward magnetic field perturbation, $\delta B_l^E$ (after the international geomagnetic reference field IGRF has been subtracted; see green curve in Figure 1d), increases gradually from 2211:30UT (leftmost vertical dashed line) to 2212:39UT (magenta vertical dashed line). This is not a temporal variation, but a spatial variation observed by the spacecraft as it traveled poleward from 67.6° to 71.7° magnetic latitude. This variation results from an east-west elongated downward FAC sheet, the R2 current in the dusk sector. From 71.7° to 74.5° magnetic latitude (2212:39UT to 2213:27 UT; magenta vertical dashed line to rightmost vertical dashed line), $\delta B_l^E$ drops gradually. This drop results from an east-west elongated upward FAC sheet, the R1 current.

According to Ampère's law, the steeper the slope of $\delta B_l^E$, the larger the current density; the larger the $\delta B_l^E$ change, the more FACs produce this change (e.g., Lühr et al., 1996). Within the expanses of R1 and R2 currents, $\delta B_l^E$ slopes of various field change, steepness, and latitudinal widths exist (Figure 1d), indicating that the R1 and R2 currents contain secondary FACs of various current content, intensity, and scales. These FACs are commonly observed within R1 and R2 currents (Gjerloev et al., 2011; Klumpar, 1979; Lühr et al., 2015; McGranaghan et al., 2017). In this paper, we discuss one previously unrecognized type of secondary FAC that has a mesoscale latitudinal expanse (>~0.5° and <~5°) and carries more than 30% of the total R1 or R2 current. Such FACs may be important for resolving the global current system and understanding convection of the magnetosphere and ionosphere during active times (see Section 4).

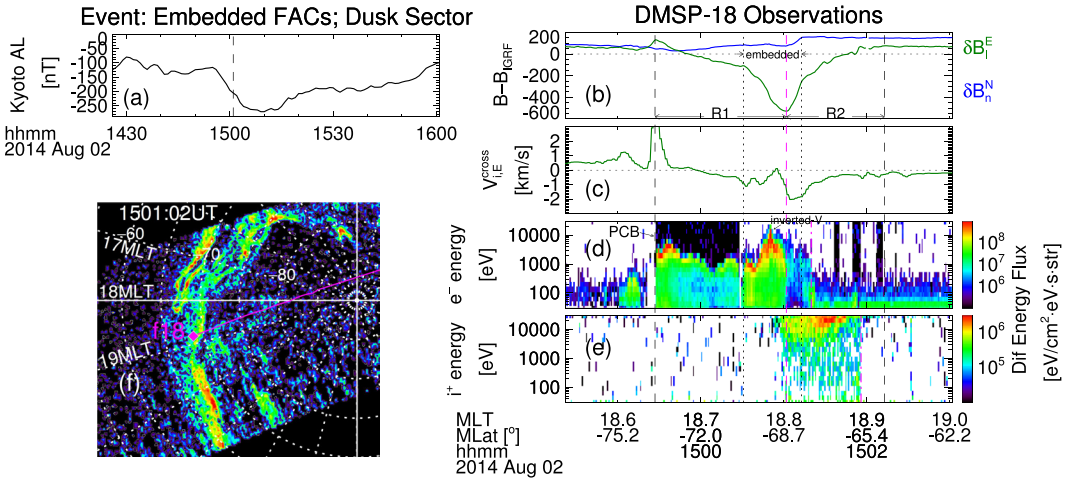


**Figure 2.** An embedded FAC event observed by DMSP-18 in the dusk sector. (a) Kyoto AL index. The vertical dashed line indicates 1501:02UT, the time at which the spacecraft crosses the R1/R2 interface. (b) The same quantities as in Figure 1d. Vertical dotted lines indicate the boundaries of embedded FACs. The other lines are as defined for Figure 1d. (c) Ion bulk flow, cross-track component, approximately eastward. Magenta vertical dashed-dotted line: polar cap boundary. (d and e) Differential energy flux of precipitating electrons and ions. Magenta vertical dashed-dotted lines are the equatorward boundaries of the electron and ion plasma sheets, respectively. (f) Ultraviolet auroral emissions from SSUSI. Redder color: more intense light flux. Dashed grids: magnetic latitudes and MLTs. Magenta line: DMSP-18 track and diamond: the spacecraft location at 1501:02UT, August 2, 2014.

In Figure 2, we introduce this type of FAC, which was observed by the DMSP-18 spacecraft as it transected R1 and R2 currents with an equatorward trajectory in the dusk sector of the southern hemisphere. Using the method we applied in Figure 1d, we identify in Figure 2b that the upward R1 current corresponds to a $\delta B_l^E$ decrease from −73.7° to −68.6° magnetic latitude (1459:27UT to 1501:02UT; from the leftmost vertical dashed line and the magenta dashed line), and the downward R2 current corresponds to a $\delta B_l^E$ increase from −68.6° to −64.7° magnetic latitude (1501:02UT to 1502:13UT; from the magenta dashed line to the rightmost vertical dashed line). Figure 2b shows a feature within the latitudinal range of the R1 (R2) current that Figure 1d does not: $\delta B_l^E$ can be further split into two segments with distinctly different slopes; the splitting boundary is indicated by the vertical dotted line at 1500:31UT (1501:13UT). The split segments are thus as follows: 1459:27UT to 1500:31UT and 1500:31UT to 1501:02UT for R1; 1501:02UT to 1501:13UT and 1501:13UT to 1502:13UT for R2. These segments all have a mesoscale latitudinal extent (>0.5°, but less than the full width of the R1 and R2 currents) and a large field change (>20% of the total change over the R1 or R2 current's latitudinal range). Within the R1 range, the segment from 1500:31UT to 1501:02UT, which is adjacent to the R1/R2 interface (magenta dashed line), has a much steeper slope than that farther away (the segment from 1459:27UT to 1500:31UT). The slopes of the two segments have the same sign, however. It is also so within the R2 range—the 1501:02UT to 1501:13UT slope is much steeper than and has the same sign as the 1501:13UT to 1502:13UT slope. These signatures indicate that the FAC responsible for the steeper segment within the R1 (R2) range has the following characteristics:

1. It flows in the same direction as the R1 (R2) current.
2. It is more intense than the background R1 (R2) current, which corresponds to the segment with a gentler slope farther away from the R1/R2 interface.
3. Of all meso- and large-scale FACs within the R1 (R2) range, it flows closest to the R1/R2 interface.

The steeper segments (one within R1 range and one within R2 range) appear to be embedded in the middle of the total latitudinal range covered by the R1 and R2 currents (1459:27UT to 1502:13UT). We thus refer to the FAC responsible for the steeper segment within the R1 (R2) range as an "embedded R1 (R2) FAC." Characteristics 1–3 define this term.

Our experience in finding the events presented in this paper suggests that embedded R1 and R2 FACs occur frequently and are worthy to be established as a notable feature of magnetosphere-ionosphere system.

These FACs may result in some ionospheric $B_E$ deflections previously shown (e.g., Fukunishi et al., 1993; Iijima & Potemra, 1976b; Klumpar et al., 1976; Liu et al., 2018; Saflekos et al., 1982; Strangeway, 2012), but these studies did not discuss them or point out their possible importance. We can infer their significance from other studies, however. Using the global FAC map from AMPERE (Active Magnetosphere and Planetary Electrodynamics Response Experiment) fit data (e.g., Anderson et al., 2000), Clausen et al. (2013) showed that a substorm current wedge (SCW), the most significant current system in substorms (McPherron et al., 1973), arises in the equatorward portion of the R1 current. This location indicates that the SCW most likely originates as an embedded R1 FAC. Therefore, embedded FACs may be important for understanding the substorm current system.

The AMPERE technique effectively averages low-resolution measurements over time, so it cannot resolve fine properties of embedded FACs. Therefore, we rely on single passes of low-altitude spacecraft to examine typical embedded R1 and R2 events in detail (Section 3) and establish them as a distinctive feature. We propose a possible mechanism that produces them in Section 4.

## 2. Data Set

The embedded FAC events we examine come from observations of DMSP and Swarm spacecraft at altitudes of ~840 km and 460–530 km, respectively. These spacecraft make in-situ measurements of ionospheric parameters, including the magnetic field vector (Merayo et al., 2008; Rich, 1984) and the cross-track (in the horizontal plane and perpendicular to the spacecraft trajectory) ion bulk flow (Knudsen et al., 2017; Rich & Hairston, 1994). The DMSP spacecraft also measure 30 eV–30 keV ion and electron precipitation (e.g., Hardy et al., 2008).

When transecting the latitudes of the auroral oval, these spacecraft have trajectories that are usually approximately perpendicular to constant magnetic latitude lines, and correspondingly to the elongation orientation of large-scale R1 and R2 current sheets (Figure 1a). Such trajectories are ideal for observing magnetic field variations caused by R1 and R2 currents (e.g., Fung & Hoffman, 1992). When in the auroral zone, DMSP covers the dawn and dusk MLTs best, and Swarm covers all MLTs equally well.

Because the spacecraft transect the auroral oval very quickly (within a few minutes), we treat all meso- and large-scale variations in the temporal series of spacecraft data as spatial variations with magnetic latitude (e.g., Figures 1d and 2b).

The R1 and R2 current sheets do not align exactly with magnetic latitude lines. Thus, their corresponding magnetic variations appear in both the east-west and north-south components. To best present the variations, we show the horizontal magnetic field in a coordinate system formed by the maximum and minimum field variation directions over the latitudinal range occupied by R1 and R2 currents (these two directions are perpendicular to each other). We compute these directions by applying principal component analysis (PCA) (Pearson, 1901) to the two-component horizontal field. Of the two opposite possible maximum (minimum) directions, we choose the one closer to the eastward (northward) direction. We denote the magnetic field components in the maximum and minimum variance directions as $\delta B_l^E$ and $\delta B_n^N$, respectively (IGRF has been subtracted before applying PCA). For the events in this paper, the angles between the maximum variation **l** and the magnetic eastward directions (and thus between the minimum variation **n** and the magnetic northward directions) are small: 6°, 6°, 3°, 6°, 7°, and 2° for the events shown in Figures 1–5, respectively. Thus, we still refer to the maximum and minimum variation directions as east-west and north-south, respectively. We do not show the vertical field component because it is little affected by R1 and R2 currents, which are nearly vertical.

The ion bulk flow we present is $V_{i,E}^{\text{cross}}$, the horizontal component perpendicular to the spacecraft trajectory and positive in the direction closer to eastward. Because the spacecraft trajectories are approximately perpendicular to the east-west direction, we will refer to $V_{i,E}^{\text{cross}}$ as eastward flow. To remove any offset in the flow data we show, we subtracted the average value within an unperturbed interval below the R2 current latitude, where the flow is expected to vanish.

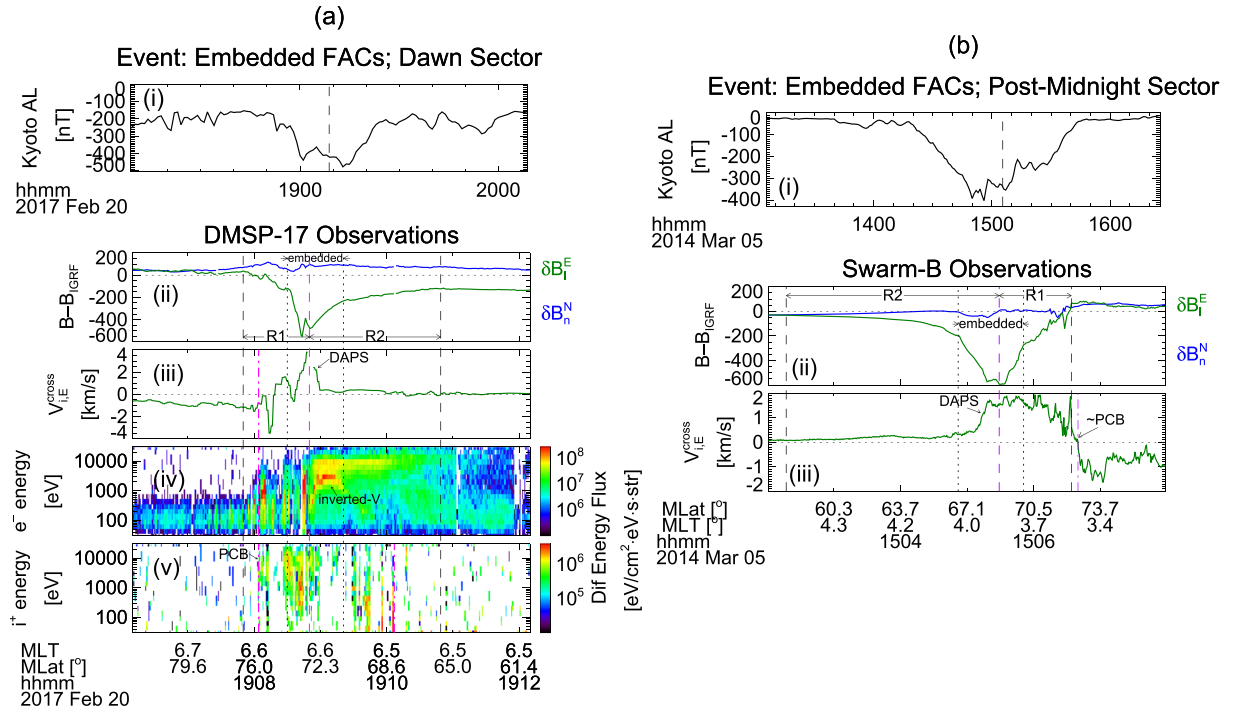


**Figure 3.** Embedded FAC events observed in the (a) dawn and (b) post-midnight sectors. (ai and bi) Kyoto AL index. The vertical dashed lines indicate 1908:50UT and 1505:29UT, respectively. (aii and bii) The same quantities as in Figure 2b. The vertical dashed and dotted lines have the same meaning as those in Figure 2b. (aiii, biii, aiv, and av) The same quantities as in Figures 2c–2e, respectively. The magenta vertical dash-dotted line at 1908:04UT in panels aiii–av indicates the polar cap boundary; that in panel biii indicates the approximate location of the PCB. The magenta vertical dash-dotted line at 1910:07UT corresponds to the equatorward boundary of the ion plasma sheet.

We will investigate how embedded FACs are related to auroral forms, which we identified from images of the SSUSI (Spectral Sensor Ultraviolet Spectrographic Imager) onboard each DMSP spacecraft (Paxton et al., 2018) and the THEMIS (Time History of Events and Macroscale Interactions during Substorms) all-sky

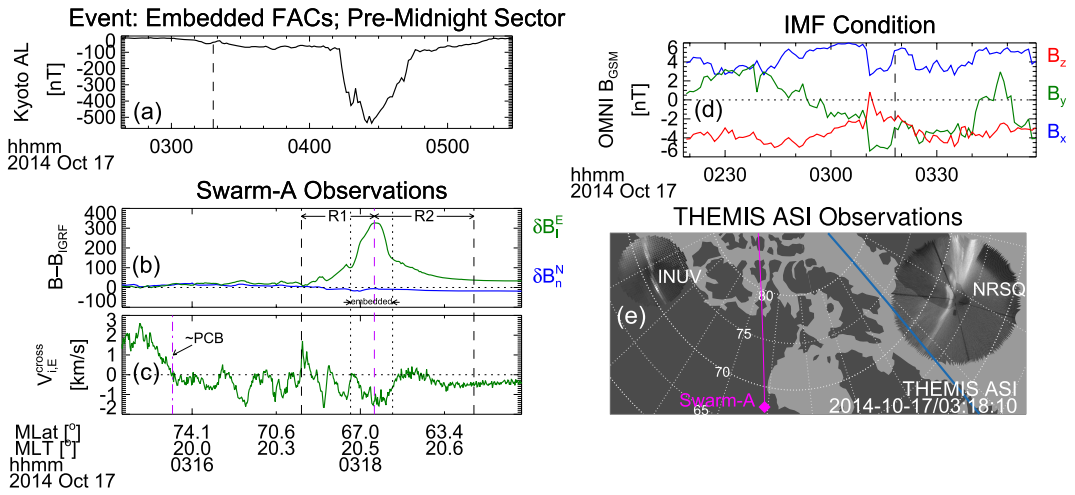


**Figure 4.** An embedded FAC event observed by Swarm-A in the pre-midnight sector. (a–c) The same quantities as Figures 3bi–3biii. All vertical lines have the same meaning as those in Figures 3bi–3biii. (d) Interplanetary magnetic field from OMNI, in GSM coordinate system. The vertical dashed line indicates 0318:10UT. (e) White-light auroral images from THEMIS All-Sky Imagers at Inuvik (INUV) and Narsaq (NRSQ). Circle-like areas: the fields of view of the ASIs. Whiter color in the circle-like areas: more light flux. White dotted grids: invariant latitudes and longitudes. Blue line: midnight. Magenta line and diamond: Swarm-A track and location, respectively, at 0318:10UT, October 17, 2014.

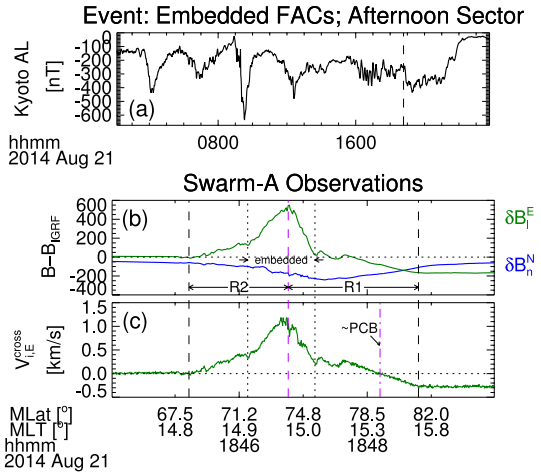


**Figure 5.** An embedded FAC event observed by Swarm-A in the afternoon sector. (a–c) The same quantities as Figures 3bi–3biii. All vertical lines have the same meaning as those in Figures 3bi–3biii.

imagers (ASIs) (Mende et al., 2008). The SSUSI records ultraviolet auroral emissions from below the spacecraft, whereas THEMIS ASIs take white-light photos of the sky above from their positions on the ground. When plotting spacecraft projections on auroral images (Figures 2f and 4e), we map the spacecraft locations along magnetic field lines to an assumed auroral altitude of 110 km, a commonly used value for white-light and ultraviolet aurorae. All the spacecraft locations (magnetic latitude and MLT) we mention in this paper are such mapped values.

## 3. Embedded FAC Events

### 3.1. Dusk Sector Event

Now we return to Figure 2, which describes an event that occurred when AL equaled −205 nT and was decreasing, later reaching −270 nT (Figure 2a). The AL values and profile indicate that this event likely occurred during a substorm expansion phase. As mentioned in Section 1, the dashed and dotted vertical lines in Figure 2b split the R1 and R2 range into four separate segments, each corresponding to an FAC sheet (from left to right): background R1, embedded R1, embedded R2, and background R2. Although the embedded FACs may be understood as superimposed on top of background FACs, we do not adopt this understanding (except when discussing Figure 3aiv). Instead, we define the four segments in the simplest way: they do not overlap, and each segment is treated as one FAC when discussing its latitudinal width, current content, and current density. Table 1 lists the latitudinal widths of the four segments. The embedded FACs are >0.5° wide, of the same order of magnitude as the latitudinal widths of the background FACs. The latitudinal widths of the embedded FACs are thus indeed mesoscale (>0.5° and <5°), and this is the case for all the embedded FAC events in this study (MLat width column of Table 1).

Although the field variations in all four segments are mainly eastward-westward (green component in Figure 2b), within some segments the FAC also generates a change in $\delta B_n^N$. The FAC sheets are thus not exactly eastward-westward elongated. To determine the orientation of the FAC sheet in each segment, we apply PCA to the horizontal field within the segment and denote the maximum and minimum directions as $\mathbf{l}'$ and $\mathbf{n}'$, respectively. The ratio of the eigenvalues of these two directions is >10 for every segment; this is true for all events presented in this paper ($\lambda_{l'}/\lambda_{n'}$ column of Table 1). Thus, the field variation in every segment corresponds to a well-defined current sheet transected by the spacecraft, rather than to a remote effect from currents elsewhere (Fung & Hoffman, 1992; Hoffman et al., 1994). The current sheets' elongation direction is $\mathbf{l}'$. The angles between $\mathbf{l}'$ and magnetic east are listed in the $|\theta_{l'E}|$ column of Table 1. According to this column, the angles for Figure 2's event, as well as those for all other events in this study, are small (all <31°). All the FAC segments in this paper are thus mainly elongated in the magnetic east-west direction.

In Figure 2b, the embedded FAC is responsible for 64% (45%) of the total $\delta B_l^E$ change, and thus also of the FAC content, over the entire R1 (R2) range at the MLT traveled by the spacecraft. The percentages for FAC content are approximations because the FAC sheet in each $\delta B_l^E$ segment is not exactly parallel to $\mathbf{l}$. To compute the content more accurately, we project the horizontal field within each segment to its $\mathbf{l}'$ direction to get $\delta B_{l'}$. The content, $i$, is then given by $\Delta\delta B_{l'} / \mu_0$, where $\Delta\delta B_{l'}$ is the change in $\delta B_{l'}$ over the segment. The physical meaning of $i$ is the amount of FAC within an FAC sheet per unit length in its elongation direction, $\mathbf{l}'$. In Table 1 (current content column) we list $i$ separately for the background FAC and the embedded FAC. The table shows that for all our events, including the one in Figure 2, the current content per unit length of the embedded FACs is greater than or comparable to that of the background segments.

Next, we compute the average current density j of each FAC segment as $i / d_{n'}$, where $d_{n'}$ is the current sheet thickness. For each segment, $d_{n'}$ equals the distance the observing spacecraft travels in the $\mathbf{n}'$ direction within that segment. As listed in Table 1, the current densities of the embedded FACs are systematically several times larger than those of the background FACs for all events, including the one plotted in Figure 2.

**Table 1**
*Properties of the Events Presented in This Study*

| Event | MLT | | Region | MLat width [°] | $\lvert\theta_{l'E}\rvert$ | $\lambda_{l'}/\lambda_{n'}$ | Current content (A/m) | Current density ($\mu A/m^2$) |
|---|---|---|---|---|---|---|---|---|
| Figure 1 | 19.4 | | R1 | 2.8 | 3.2 | 37 | 0.12 | 0.31 |
| | | | R2 | 4.1 | 5.5 | 91 | 0.10 | 0.19 |
| Figure 2 | 18.8 | R1 | Background | 3.4 | 12.2 | 40 | 0.19 | 0.41 |
| | | | Embedded | 1.7 | 3.7 | 790 | 0.33 | 1.55 |
| | | R2 | Embedded | 0.6 | 21.1 | 1,226 | 0.22 | 3.29 |
| | | | Background | 3.3 | 3.0 | 1,042 | 0.27 | 0.63 |
| Figure 3a | 6.6 | R1 | Background | 2.5 | 11.9 | 13 | 0.13 | 0.40 |
| | | | Embedded | 1.2 | 4.1 | 154 | 0.28 | 1.67 |
| | | R2 | Embedded | 1.9 | 7.2 | 253 | 0.19 | 0.76 |
| | | | Background | 5.3 | 2.9 | 47 | 0.09 | 0.12 |
| Figure 3b | 3.9 | R1 | Background | 2.3 | 2.4 | 20 | 0.27 | 0.90 |
| | | | Embedded | 1.2 | 6.7 | 441 | 0.26 | 1.70 |
| | | R2 | Embedded | 2.1 | 6.9 | 82 | 0.32 | 1.26 |
| | | | Background | 8.9 | 24.5 | 43 | 0.13 | 0.15 |
| Figure 4 | 20.5 | R1 | Background | 2.1 | 13.6 | 62 | 0.07 | 0.29 |
| | | | Embedded | 1.0 | 4.0 | 787 | 0.18 | 1.38 |
| | | R2 | Embedded | 0.8 | 6.5 | 4,411 | 0.15 | 1.46 |
| | | | Background | 3.5 | 2.8 | 4,540 | 0.08 | 0.19 |
| Figure 5 | 15.0 | R1 | Background | 5.8 | 30.9 | 107 | 0.17 | 0.24 |
| | | | Embedded | 1.5 | 7.1 | 471 | 0.42 | 2.22 |
| | | R2 | Embedded | 2.3 | 9.1 | 144 | 0.34 | 1.14 |
| | | | Background | 3.4 | 10.3 | 199 | 0.11 | 0.25 |

*Note*. The magnetic local time (MLT) is of the spacecraft when it is at the R1/R2 interface. The magnetic latitudinal widths are mapped values at 110 km altitude; current content and density are values at the spacecraft altitude. Note that "background" and "embedded" refer to individual latitudinal segments that do not overlap (see Section 3.1).

Figures 2c–2e display other quantities that put the FACs into context. The ion bulk flow has a westward peak (1501:05UT; Figure 2c) near the R1/R2 interface. This is the expected convection direction in the dusk sector (e.g., Heppner, 1977; Sugiura et al., 1982). The westward flow within the embedded R1 current is much slower than that in the embedded R2 current. This is because the conductivity within the embedded R1 current is too high to allow a large electric field, and thus flow (otherwise the Pederson current there will be too strong to close). The high conductivity results from an inverted-V electron precipitation (Frank & Ackerson, 1971) coinciding with the embedded R1 current (1500:50UT, Figure 2d). This inverted-V precipitation is the carrier of the upward embedded R1 current and expectedly (e.g., Kamide, 1982) corresponds to a discrete auroral arc (Figure 2f; the yellow-to-orange arc immediately poleward of the spacecraft). In contrast, Figure 1e does not show a clear inverted-V precipitation adjacent to the R1/R2 interface, and an upward embedded FAC is absent. Figure 2e shows that the downward embedded and background R2 currents are contributed by precipitating ions. These ions are of higher energy than those in the downward R2 range of Figure 1f. The higher energy is expected for active time when the plasma sheet is hotter (e.g., Wang et al., 2009). Aside from the energy difference, the ion precipitation in Figure 2e looks like that in Figure 1f. We cannot identify a distinctive feature of ion precipitation for the downward embedded FAC because downward FACs are predominately carried by upgoing electrons (Arnoldy & Choy, 1973; Kamide & Rostoker, 1977; Lui et al., 1977).

The region of precipitation corresponds to the latitudinal range of the plasma sheet. The poleward edge of the plasma sheet, the polar cap boundary (PCB), is observed by the equatorward-moving DMSP-18 at

1459:27UT, where Figure 2d shows an all-energy cutoff of electron precipitation. The PCB coincides with the poleward boundary of the R1 current. The equatorward edge of the electron plasma sheet is given by the sharp cutoff of >500 eV electron precipitation at 1501:20UT (magenta vertical dashed-dotted line in Figure 2d). The equatorward edge of the ion plasma sheet is at the all-energy cutoff of ion precipitation at 1501:56UT (magenta vertical dash-dotted line in Figure 2e). The boundaries between background and embedded FACs are within the plasma sheet; in the R2 current this boundary is near the inner edge of the electron plasma sheet.

Within the polar cap, the overall $\delta B_l^E$ slope is distinctly different from the poleward-most segment of the R1 current, which has a cleanly defined poleward boundary. Thus, the background R1 current is determined without any ambiguity that may come from polar cap $\delta B_l^E$ slopes caused by penetration of $B_{yGSM}$ from the interplanetary magnetic field to the magnetosphere (McDiarmid et al., 1979). This is true for all events in this paper.

At the PCB, there is a strong eastward flow (Figure 2c). Immediately poleward of the PCB, $\delta B_l^E$ increases (Figure 2b), signifying a downward FAC. Immediately equatorward of the PCB, the $\delta B_l^E$ slope is a little steeper than that further equatorward, indicating a strong upward FAC carried by the inverted-V precipitation at the same location (Figure 2d). These signatures all suggest the presence of a poleward boundary (of the auroral zone) arc or intensification, which is not directly related to the embedded FACs and thus out of the scope of this paper.

### 3.2. Dawn Sector Event

In the event illustrated in Figure 3a, equatorward-moving DMSP-17 transects the auroral zone at ~6.6MLT in the northern hemisphere. Around the time of this event, the AL index in Figure 3ai shows a negative bay with a minimum value of ~−480 nT. Thus, the event likely occurred during a well-developed substorm. The $\delta B_l^E$ profile in Figure 3aii shows that the downward R1 (upward R2) current occupies a magnetic latitude range from 76.6° to 72.9° (72.9° to 65.7°), or from 1907:50UT to 1908:50UT (1908:50UT to 1910:49UT). Embedded R1 and R2 currents are present from 74.1° to 71° magnetic latitude (1908:30UT to 1909:21UT). The location of the R1/R2 interface is ambiguous from the variation of $\delta B_l^E$ alone, as there are two $\delta B_l^E$ minima (1908:42UT and 1908:50UT) within the time interval of interest. We thus refer to Figure 3aiv and choose 1908:50UT, which separates structured (before this time and covering R1 range) from relatively unstructured (after this time and covering R2 range) electron precipitation, as the R1/R2 interface (Ohtani et al., 2010). The relatively unstructured precipitation does contain one structure—an inverted-V precipitation around 1909:05UT, the latitudinal extent of which coincides with that of the upward embedded R2 current. The electron precipitation within the R2 current seems to consist of two components: the inverted-V precipitation with an ~3 keV peak energy carries the embedded R2 current and is superimposed on the background R2 current carried by an unstructured precipitation with a center energy of ~10 keV. The latter is present over the entire R2 range including the range of the embedded FAC. Although it is difficult to identify the equatorward boundary of the electron plasma sheet, we can determine the ion plasma sheet boundary to be around the precipitation cutoff at 1910:07UT (68.2° magnetic latitude; Figure 3av). The polar cap boundary is at the poleward cutoff of both electron and ion precipitation (1908:04UT or 75.7° magnetic latitude, denoted by the magenta vertical dashed-dotted lines in Figures 3aiv and 3av). Thus, the plasma sheet contains the two boundaries separating background and embedded FACs.

The plasma bulk flow near the R1/R2 interface has a strong eastward peak and a steep flow gradient (Figure 3aiii); the latter is within the range of the embedded R2 current. The flow equatorward of the gradient almost vanishes. These signatures suggest that the strong eastward flow is a dawnside auroral polarization stream (DAPS, Liu et al., 2020). It is expected to appear immediately poleward of an inverted-V electron precipitation (Figure 3aiv), which in this case is the carrier of the embedded R2 current. Poleward of the DAPS and equatorward of the PCB, the bulk flow goes westward twice, opposite to the expected eastward convection at this MLT. These flows are related to the narrow inverted-V electron precipitations in Figure 3aiv and the ion precipitation gaps in Figure 3av. The flows are likely associated with auroral streamers (Gallardo-Lacourt et al., 2014; Sergeev et al., 2004), ionospheric footprints of bursty bulk flows (Angelopoulos

et al., 1992, 1994) carried by dipolarizing flux bundles (DFBs; Liu et al., 2014) in the magnetotail (e.g., Nakamura et al., 2001; Wang, Xing, et al., 2018).

### 3.3. Post-Midnight Sector Event

Figure 3b shows an event during a substorm (Figure 3bi; AL = ∼−350 nT within a cleanly defined negative bay). Poleward-moving Swarm-B transected the R2 and R1 currents at ∼4 MLT. The $\delta B_l^E$ variation in Figure 3bii indicates that the R2 and R1 currents span 57.8° to 72.3° magnetic latitude (1502:17UT to 1506:34UT), including the embedded R2 and R1 currents covering 66.7° to 70° magnetic latitude (1504:52UT to 1505:51UT). Within the range of the embedded R2 current, there is a steep flow gradient associated with a DAPS (Figure 3biii). We rely on the flow profile in Figure 3biii to determine the PCB location, because Swarm does not provide precipitation measurements. At 1506:40UT (72.7° magnetic latitude), the flow reverses from eastward as expected in the return-flow region to westward as expected in the polar cap. This flow reversal marks the equatorward limit of the PCB because the higher-latitude portion of the plasma sheet boundary layer sometimes has the same flow direction as the polar cap (e.g., Lester et al., 1995). This equatorward limit of the PCB is 2.7° poleward of the boundary between embedded and background R1 currents, so the latter boundary is within the plasma sheet. This is also true for all the following events.

### 3.4. Pre-Midnight Sector Event

Figure 4 shows an event observed by equatorward-moving Swarm-A when it transected the auroral zone at ∼21 MLT. The R1 and R2 currents range from 69.5° to 62.1° magnetic latitude (0317:18UT to 0319:21UT), and the embedded FACs cover 67.4° to 65.6° magnetic latitude (0317:53UT to 0318:23UT). Within the expanse of the R1 and R2 currents, the plasma bulk flow is mostly westward (Figure 4c), consistent with the return flow in the premidnight sector. Within the expanse of the embedded R1 and R2 currents is a westward flow peak of ∼1.5 km/s. The flow poleward of the embedded R1 current turns eastward occasionally, possibly due to auroral streamers. The flow is constantly eastward poleward of 75° magnetic latitude (0315:46UT), so this location is likely the equatorward limit of the PCB.

One feature distinguishing this event from all other embedded FAC events in this paper is that it was not observed during an active AL level—AL was only ∼−40 nT (Figure 4a). About 55 min after the event, a cleanly defined AL negative bay indicates that a substorm took place, so the event likely occurred during a substorm growth phase. Two signatures confirm this likelihood: at the time of the event, the interplanetary magnetic field has been almost constantly southward for an hour (Figure 4d), and a global discrete arc, the growth phase arc (Akasofu, 1964), was observed by two THEMIS ASIs (Figure 4e; all other ASIs' fields of view were covered by clouds). Although the |AL| level is low around the time of the event, a small peak of ∼50 nT appears at 0317UT (Figure 4a), <1 min before Swarm-A observed the embedded FACs. This small peak indicates westward ionospheric currents, which may be connected to small-scale FACs carried by DFBs (e.g., Lyons et al., 2012). The DFBs may have driven the growth phase arc (Yang et al., 2014).

### 3.5. Afternoon Sector Event

In Figure 5, the poleward-moving Swarm-A transects the auroral zone at ∼15 MLT, when the magnetosphere has been geomagnetically active for >15 h (Figure 5a). The R2 (R1) current, indicated by $\delta B_l^E$ in Figure 5b, occupies the magnetic latitude range 68.3° to 74° (74°–81.3°) or 1845:13UT to 1846:46UT (1846:46UT-1848:48UT) in the spacecraft observations. There is an embedded R2 (R1) current from 71.6° to 74° (74°–75.5°) or 1846:08UT to 1846:46UT (1846:46UT–1847:11UT). The plasma flow profile (Figure 5c) follows that of $\delta B_l^E$, indicating little, gently varying conductivity over the latitude range covered by R1 and R2 currents (Liu et al., 2020; Sugiura et al., 1982; Strangeway, 2012). This is because the entire range of R1 and R2 currents is sunlit, and the solar zenith angle ranges from 72° to 82°.

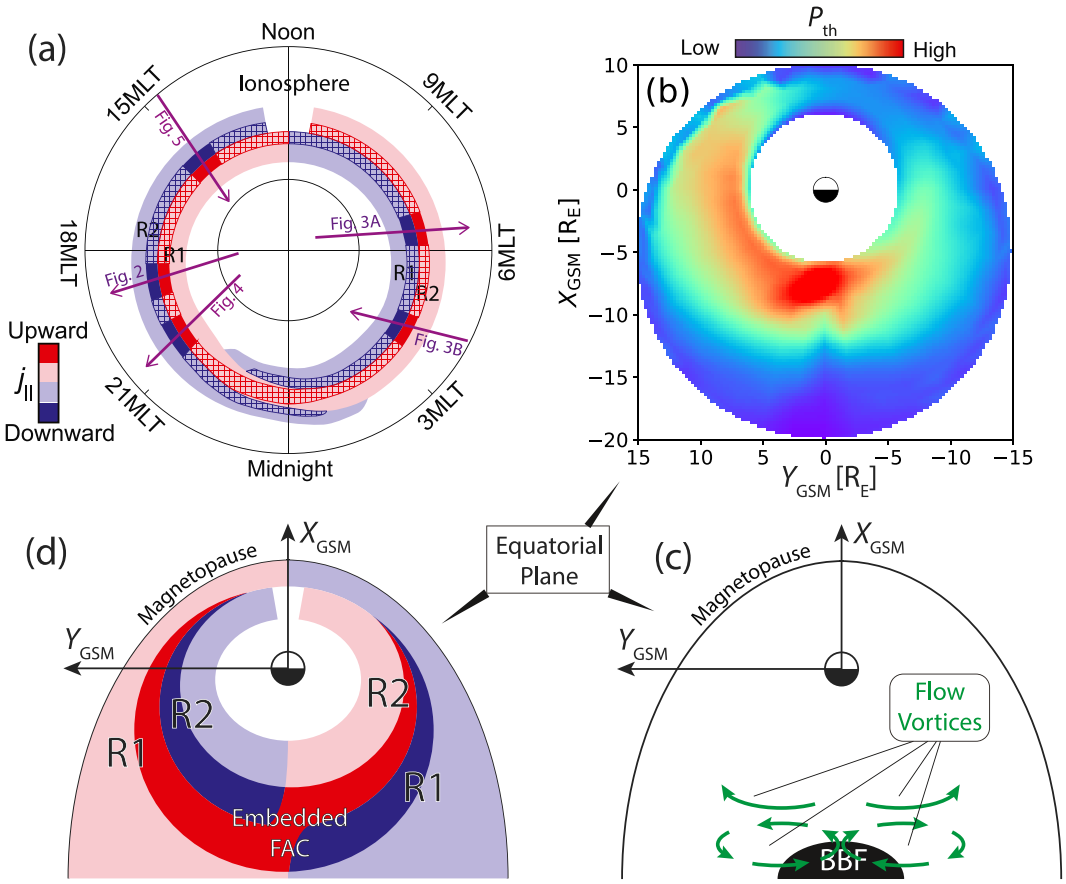


**Figure 6.** (a) Cartoon summarizing aspects of the embedded FAC events in Figures 2–5, arranged in the same way as Figure 1a. Darker colors: more intense FAC. Lines with arrowheads: schematic spacecraft trajectory of each embedded FAC event. The direction of the arrowhead is the spacecraft's direction of motion. The gridded areas indicate that the embedded FACs can be either global or localized. The in situ observations cannot establish the longitudinal extent of the events. (b–d) Schematics illustrating the equatorial plane under the condition of enhanced magnetotail convection. They are based on previous simulations of nominal convection enhancement. (b) Pressure buildup and (c) flow vortices that appear in the near-Earth plasma sheet. Green arrows indicate plasma bulk flows. The flow vortices are caused by a braking BBF, whose equatorial cross section is shown as the black area. (d) Similar to Figure 1b but with the addition of embedded FACs; darker colors represent the equatorial footprints of more intense FACs.

## 4. Summary and Discussion

Figure 6a is an illustrative summary of the embedded FAC events we presented. Although a more extensive statistical study is needed for confirmation, these five events suggest that embedded FACs have the following properties:

1. The transitions from weak background R1 (R2) FAC to strong embedded R1 (R2) FAC, and thus the boundaries of the embedded FACs, are within the plasma sheet.
2. The embedded FACs are independent of ionospheric conditions—they can appear in both dark and sunlit regions. This suggests that they likely result from "current generators" (Nishida, 1979) in the magnetosphere. A current generator is the expected generator for structures with spatial scales similar to those of embedded FACs (Vickrey et al., 1986).
3. It seems that embedded FACs occur preferentially during active times or substorm growth phase, and on field lines that cross the equator on the night side. Except in the event in Figure 5, all the events we have presented can be mapped to an equatorial location in the nightside magnetosphere (even the event in Figure 3a, observed at 6.5 MLT, maps to the nightside because of field line draping).
4. An upward embedded FAC, which is carried by electron precipitation with an inverted V shape, links to a discrete arc. This relationship is also present in the embedded FACs we can identify from previous

studies such as those in Figures 2 and 3 of Liu et al. (2020) (the embedded FACs can be identified from the magnetic field variations in these figures; their Figure 3 does not show a clean embedded R1 FAC) and Figure 1 of Liu et al. (2018). Thus, an upward embedded FAC is so strong that field-aligned potential drops develop (Evans, 1974; Lyons, 1981) to support it.

5. When appearing in the postmidnight-to-dawn sector, the embedded R2 current coincides with a DAPS. This is also so for the events in Liu et al. (2018, 2020). This coincidence further supports the idea that embedded FACs result from a current generator, because a DAPS results from a current generator (Liu et al., 2020).

These properties inspire us to propose a mechanism for generating embedded FACs based on previous simulations. After magnetotail convection increases, plasma pressure builds up in the plasma sheet, especially in the region of $L = 6$–$15$ (schematically illustrated in Figure 6b; see, e.g., Birn & Hesse, 2013; Gkioulidou et al., 2009; Wang, Gkioulidou, et al., 2018; Yang et al., 2010). This buildup can result from either enhanced global-scale convection or bursty bulk flows carried by DFBs. The latter also produce flow vortices around them (Figure 6c; Birn et al., 1999, 2004). According to theory (Vasyliunas, 1970) and the simulations cited above, the pressure buildup and flow vortices in Figures 6b and 6c require intense R1 and R2-sense FACs to arise in the near-Earth plasma sheet; the distribution of such FACs is illustrated as darker areas in Figure 6d (see also the cited simulation studies). The near-Earth plasma sheet is also where the large-scale R1/R2 interface is located (Liu et al., 2016); the intense FACs are simulated to appear near this interface and redefine it as the interface between the intense R1 and intense R2 FACs. Flowing toward or away from the ionosphere along field lines, these intense FACs would produce the magnetic field deflections we observed and identified as signifying embedded FACs. In addition, the location of these intense FACs relative to the plasma sheet is consistent with that of embedded FACs. When mapped to the ionosphere, the simulated intense FACs have current densities comparable to those we observed for embedded FACs (Gkioulidou et al., 2009; Yang et al., 2012, 2014). They are therefore a plausible candidate for embedded FACs.

The mechanism illustrated in Figure 6 results from enhanced convection, a condition present during high |AL| periods and substorm growth phases, when the embedded FAC events in Figures 2–5 were observed. The pressure buildup and flow vortices start in the magnetotail, so the embedded FACs should be best observed on the nightside. The pressure buildup then drifts to the afternoon sector (Gkioulidou et al., 2009; Wang et al., 2019). It is thus unsurprizing to observe some embedded FACs in the afternoon sector (Figure 5).

The mechanism in Figure 6 has also been used to explain how DAPS arise (Liu et al., 2020), so embedded R2 FACs in the postmidnight-to-down sector are expected to coexist with DAPS. In fact, a strong R2 FAC is suggested to be the direct driver of DAPS. Because DAPS are important for convection, plasma heating, and instabilities in the magnetosphere-ionosphere-thermosphere system, it is also important to understand embedded FACs.

In Figure 3a, a DAPS and embedded FACs are observed with flows likely related to streamers, consistent with DFBs being one driver of magnetotail pressure buildup and flow vortices. Likely streamer-related flows also appear in Figure 4c, in which a strong westward flow coincides with embedded FACs. Because strong westward flows in the premidnight sector are known to be related to DFBs (Gallardo-Lacourt et al., 2017; Lyons et al., 2015), the event in Figure 4 lends further support to DFBs as drivers of embedded FACs.

In Figures 6b–6d, we illustrate pressure buildup, flow vortices, and intense FACs extending over a large-to-global expanse of MLTs, as in simulations (e.g., Yang et al., 2014; Wang, Gkioulidou, et al., 2018). In reality, however, these signatures and thus the associated embedded FACs may be either meso-, large-, or global-scale in MLT coverage. It is reasonable to expect embedded FACs associated with a DFB to be mesoscale in MLT coverage (i.e., <1 h of MLT wide), because a DFB's equatorial footprint is typically $<\sim 3\ R_E$ wide in the azimuthal direction (Liu, Angelopoulos, Zhou, et al., 2013; Sergeev et al., 1996). If a DFB spreads azimuthally (Liu, Angelopoulos, Zhou, et al., 2015; Wang, Gkioulidou, et al., 2018) or many DFBs cumulatively lead to large-to-global-scale modifications of the M-I system (e.g., Merkin et al., 2019), the resultant embedded FACs should have a large-to-global MLT expanse, although their latitudinal expanse would still be mesoscale. Another possible cause of global-scale embedded FACs is enhanced global-scale convection. We cannot determine the MLT expanse of the embedded FACs in Figures 2–5 from the in-situ observations of a single low-altitude spacecraft alone. During substorm growth phase (Figure 4), embedded FACs may be

large scale (>~3 h of MLT wide) because the growth phase arc, a discrete arc likely coinciding with upward embedded FACs, is usually large scale (e.g., Nishimura et al., 2016). Future studies with more approaches are needed to determine the MLT extent of embedded FACs.

Our study excluded the midnight sector where the Harang (1946) reversal complicates the definition of R1 and R2 and thus embedded R1 and R2 FACs. In addition, it will be challenging to identify embedded FACs in the midnight sector during active times, when they seem to occur more often, because this sector is much disturbed during such times (e.g., Akasofu, 1964), complicating identification of mesoscale FAC structures. Nevertheless, we can conjecture what embedded FACs would look like in this sector if the mechanism in Figure 6 is indeed responsible for them. According to simulations used to develop Figure 6 (e.g., Gkioulidou et al., 2009; Wang et al., 2020; Yang et al., 2012), embedded FACs in the midnight sector should show up as enhancements of the entire upward FAC and the lower- (higher-) latitude portion of the downward FAC poleward (equatorward) of the upward FAC. These enhanced FACs are illustrated as gridded areas in the midnight sector of Figure 6a.

Most of the events in this study were observed under high |AL| conditions during likely substorms. A high |AL| indicates that a substorm current wedge is well formed (e.g., McPherron & Chu, 2016). Because an SCW consists of an intense R1-sense FAC and an intense R2-sense FAC equatorward of the R1-sense FAC (Ritter & Lühr, 2008; Sergeev et al., 2011), it is reasonable to relate embedded R1 and R2 currents to an SCW. In fact, the mechanism in Figure 6 was designed to explain SCW formation (e.g., Birn & Hesse, 2013). There are two opposing ideas about SCW configuration: an SCW is either formed simply by two large-scale (>3 h of MLT wide) R1 and R2-sense current loops (Nishimura et al., 2020; Ohtani & Gjerloev, 2020) or by a collective effect of many co-existing wedgelets (<1 h of MLT-wide) carried by DFBs distributed in different MLTs (Birn & Hesse, 2013, 2014; Forsyth et al., 2014; Liu, Angelopoulos, Chu, et al., 2015; Liu, Angelopoulos, Runov, & Zhou, 2013; Nishimura et al., 2020). It is difficult to verify these scenarios from in situ magnetospheric observations because at any given time, sparsely distributed spacecraft can take measurements at only a few spots. Therefore, although magnetospheric observations have revealed SCW-related signatures such as pressure buildup (Liu, Angelopoulos, Zhou, et al., 2013; Xing et al., 2011; Yao et al., 2012), flow vortices (Keiling et al., 2009), and FACs (Forsyth et al., 2008; Liu, Angelopoulos, Runov, & Zhou, 2013; Sergeev et al., 1996; Sun et al., 2013), other types of observations are needed to determine how SCWs are formed. If embedded FACS are indeed related to SCWs, ionospheric observations of embedded FACs may provide a solution. Such observations can be similar to those in this paper but with multiple spacecraft separated in the longitudinal direction to resolve the FACs' MLT expanse. If an SCW has a simple structure of two large-scale loops, we expect related embedded FACs to cover >3 h of MLT continuously. If wedgelets form an SCW, related embedded FACs should be distributed separately to several locations, with each FAC covering <1 h of MLT.

Regardless of their relationship to an SCW, embedded FACs observed in the ionosphere serve as a convenient indicator of enhanced FACs in the magnetosphere. On the nightside, the embedded FACs' equatorial footprints are around $-X_{GSM} = \sim 6$–$15\ R_E$ (near where the R1/R2 interface map to; see Liu et al., 2016; Yue et al., 2015), the most important energy conversion region in the magnetotail. The embedded FACs likely play a role in the conversions. Because embedded FACs seem to appear frequently, they reflect a fundamental state of the magnetosphere-ionosphere system. Knowledge about them is significant for correctly modeling this system.

## Data Availability Statement

The data used in this study are publicly available at the Madrigal site (http://cedar.openmadrigal.org/), the Swarm Data Access site (https://swarm-diss.eo.esa.int/), the THEMIS data center (http://themis.ssl.berkeley.edu/data/themis/), the SSUSI data center (https://ssusi.jhuapl.edu/), CDA Web (https://cdaweb.gsfc.nasa.gov/), and the World Data Center for Geomagnetism, Kyoto (http://wdc.kugi.kyoto-u.ac.jp/).

**Acknowledgments**
The authors thank James Weygand, Vassilis Angelopoulos, and Anton Artemyev for useful discussions and Judith Hohl for editing. Work at UCLA was supported by Air Force MURI grant AFOSR FA9559-16-1-0364 and NASA grants 80NSSC20K1314, 80NSSC20K1316, and contract NAS5-02099. The authors thank the DMSP, Swarm, THEMIS, OMNI and Kyoto indices teams for providing data.

## References

Akasofu, S.-I. (1964). The development of the auroral substorm. *Planetary and Space Science*, *12*, 273–282. https://doi.org/10.1016/0032-0633(64)90151-5

Anderson, B. J., Takahashi, K., & Toth, B. A. (2000). Sensing global Birkeland currents with iridium engineering magnetometer data. *Geophysical Research Letters*, *27*(24), 4045–4048. https://doi.org/10.1029/2000GL000094

Angelopoulos, V., Baumjohann, W., Kennel, C. F., Coroniti, F. V., Kivelson, M. G., Pellat, R., et al. (1992). Bursty bulk flows in the inner central plasma sheet. *Journal of Geophysical Research*, *97*, 4027–4039. https://doi.org/10.1029/91JA02701

Angelopoulos, V., Kennel, C. F., Coroniti, F. V., Pellat, R., Kivelson, M. G., Walker, R. J., et al. (1994). Statistical characteristics of bursty bulk flow events. *Journal of Geophysical Research*, *99*, 21257–21280. https://doi.org/10.1029/94ja01263

Arnoldy, R. L., & Choy, L. W. (1973). Auroral electrons of energy less than 1 Kev observed at rocket altitudes. *Journal of Geophysical Research*, *78*(13), 2187–2200. https://doi.org/10.1029/JA078i013p02187

Birn, J., & Hesse, M. (2013). The substorm current wedge in MHD simulations. *Journal of Geophysical Research: Space Physics*, *118*, 3364–3376. https://doi.org/10.1002/jgra.50187

Birn, J., & Hesse, M. (2014). The substorm current wedge: Further insights from MHD simulations. *Journal of Geophysical Research: Space Physics*, *119*, 3503–3513. https://doi.org/10.1002/2014JA019863

Birn, J., Hesse, M., Haerendel, G., Baumjohann, W., & Shiokawa, K. (1999). Flow braking and the substorm current wedge. *Journal of Geophysical Research*, *104*(A9), 19895–19903. https://doi.org/10.1029/1999JA900173

Birn, J., Raeder, J., Wang, Y. L., Wolf, R. A., & Hesse, M. (2004). On the propagation of bubbles in the geomagnetic tail. *Annales Geophysicae*, *22*, 1773–1786. https://doi.org/10.5194/angeo-22-1773-2004

Clausen, L. B. N., Milan, S. E., Baker, J. B. H., Ruohoniemi, J. M., Glassmeier, K.-H., Coxon, J. C., & Anderson, B. J. (2013). On the influence of open magnetic flux on substorm intensity: Ground- and space-based observations. *Journal of Geophysical Research: Space Physics*, *118*(6), 2958–2969. https://doi.org/10.1002/jgra.50308

Cowley, S. W. H. (2000). Magnetosphere-ionosphere interactions: A tutorial review. In S.-i Ohtani, R. Fujii, M. Hesse, & R. L. Lysak (Eds.), Geophysical monograph series (pp. 91–106). American Geophysical Union. https://doi.org/10.1029/GM118p0091

Evans, D. S. (1974). Precipitating electron fluxes formed by a magnetic field aligned potential difference. *Journal of Geophysical Research*, *79*(19), 2853–2858. https://doi.org/10.1029/JA079i019p02853

Forsyth, C., Fazakerley, A. N., Rae, I. J., J. Watt, C. E., Murphy, K., Wild, J. A., et al. (2014). In situ spatiotemporal measurements of the detailed azimuthal substructure of the substorm current wedge. *Journal of Geophysical Research: Space Physics*, *119*, 927–946. https://doi.org/10.1002/2013JA019302

Forsyth, C., Lester, M., Cowley, S. W. H., Dandouras, I., Fazakerley, A. N., Fear, R. C., et al. (2008). Observed tail current systems associated with bursty bulk flows and auroral streamers during a period of multiple substorms. *Annales Geophysicae*, *26*(1), 167–184. https://doi.org/10.5194/angeo-26-167-2008

Frank, L. A., & Ackerson, K. L. (1971). Observations of charged particle precipitation into the auroral zone. *Journal of Geophysical Research*, *76*(16), 3612–3643. https://doi.org/10.1029/JA076i016p03612

Fukunishi, H., Takahashi, Y., Nagatsuma, T., Mukai, T., & Machida, S. (1993). Latitudinal structures of nightside field-aligned currents and their relationships to the plasma sheet regions. *Journal of Geophysical Research*, *98*(A7), 11235. https://doi.org/10.1029/92JA02031

Fung, S. F., & Hoffman, R. A. (1992). Finite geometry effects of field-aligned currents. *Journal of Geophysical Research*, *97*(A6), 8569. https://doi.org/10.1029/91JA03026

Gallardo-Lacourt, B., Nishimura, Y., Lyons, L. R., Mishin, E. V., Ruohoniemi, J. M., Donovan, E. F., et al. (2017). Influence of auroral streamers on rapid evolution of ionospheric SAPS flows. *Journal of Geophysical Research: Space Physics*, *122*(12), 406–412. https://doi.org/10.1002/2017ja024198

Gallardo-Lacourt, B., Nishimura, Y., Lyons, L. R., Zou, S., Angelopoulos, V., Donovan, E., et al. (2014). Coordinated SuperDARN THEMIS ASI observations of mesoscale flow bursts associated with auroral streamers. *Journal of Geophysical Research: Space Physics*, *119*, 142–150. https://doi.org/10.1002/2013JA019245

Gjerloev, J. W., Ohtani, S., Iijima, T., Anderson, B., Slavin, J., & Le, G. (2011). Characteristics of the terrestrial field-aligned current system. *Annales Geophysicae*, *29*(10), 1713–1729. https://doi.org/10.5194/angeo-29-1713-2011

Gkioulidou, M., Wang, C.-P., Lyons, L. R., & Wolf, R. A. (2009). Formation of the Harang reversal and its dependence on plasma sheet conditions: Rice convection model simulations. *Journal of Geophysical Research*, *114*(A7). https://doi.org/10.1029/2008ja013955

Harang, L. (1946). The mean field of disturbance of polar geomagnetic storms. *Journal of Geophysical Research*, *51*(3), 353. https://doi.org/10.1029/TE051i003p00353

Hardy, D. A., Holeman, E. G., Burke, W. J., Gentile, L. C., & Bounar, K. H. (2008). Probability distributions of electron precipitation at high magnetic latitudes. *Journal of Geophysical Research*, *113*(A6). https://doi.org/10.1029/2007JA012746

Heppner, J. P. (1977). Empirical models of high-latitude electric fields. *Journal of Geophysical Research*, *82*(7), 1115–1125. https://doi.org/10.1029/JA082i007p01115

Hoffman, R. A., Fujii, R., & Sugiura, M. (1994). Characteristics of the field-aligned current system in the nighttime sector during auroral substorms. *Journal of Geophysical Research*, *99*(A11), 21303. https://doi.org/10.1029/94JA01659

Iijima, T., & Potemra, T. A. (1976a). Field-aligned currents in the dayside cusp observed by Triad. *Journal of Geophysical Research*, *81*(34), 5971–5979. https://doi.org/10.1029/JA081i034p05971

Iijima, T., & Potemra, T. A. (1976b). The amplitude distribution of field-aligned currents at northern high latitudes observed by Triad. *Journal of Geophysical Research*, *81*(13), 2165–2174. https://doi.org/10.1029/JA081i013p02165

Kamide, Y. (1982). The relationship between field-aligned currents and the auroral electrojets: A review. *Space Science Reviews*, *31*(2), 127–243. https://doi.org/10.1007/BF00215281

Kamide, Y., & Rostoker, G. (1977). The spatial relationship of field-aligned currents and auroral electrojets to the distribution of nightside auroras. *Journal of Geophysical Research*, *82*(35), 5589–5608. https://doi.org/10.1029/JA082i035p05589

Keiling, A., Angelopoulos, V., Runov, A., Weygand, J., Apatenkov, S. V., Mende, S., et al. (2009). Substorm current wedge driven by plasma flow vortices: THEMIS observations. *Journal of Geophysical Research*, *114*. https://doi.org/10.1029/2009JA014114

Klumpar, D. M. (1979). Relationships between auroral particle distributions and magnetic field perturbations associated with field-aligned currents. *Journal of Geophysical Research*, *84*(A11), 6524. https://doi.org/10.1029/JA084iA11p06524

Klumpar, D. M., Burrows, J. R., & Wilson, M. D. (1976). Simultaneous observations of field-aligned currents and particle fluxes in the rost-midnight sector. *Geophysical Research Letters*, *3*(7), 395–398. https://doi.org/10.1029/GL003i007p00395

Knudsen, D. J., Burchill, J. K., Buchert, S. C., Eriksson, A. I., Gill, R., Wahlund, J. E., et al. (2017). Thermal ion imagers and Langmuir probes in the Swarm electric field instruments. *Journal of Geophysical Research: Space Physics*, *122*, 2655–2673. https://doi.org/10.1002/2016ja022571

Lester, M., Lockwood, M., Yeoman, T. K., Cowley, S. W. H., Lühr, H., Bunting, R., & Farrugia, C. J. (1995). The response of ionospheric convection in the polar cap to substorm activity. *Annales Geophysicae*, *13*(2), 147–158. https://doi.org/10.1007/s00585-995-0147-3

Liu, J., Angelopoulos, V., Chu, X., & McPherron, R. L. (2016). Distribution of Region 1 and 2 currents in the quiet and substorm time plasma sheet from THEMIS observations. *Geophysical Research Letters*, *43*(15), 7813–7821. https://doi.org/10.1002/2016gl069475

Liu, J., Angelopoulos, V., Chu, X., Zhou, X. Z., & Yue, C. (2015). Substorm current wedge composition by wedgelets. *Geophysical Research Letters*, *42*, 1669–1676. https://doi.org/10.1002/2015GL063289

Liu, J., Angelopoulos, V., Runov, A., & Zhou, X.-Z. (2013). On the current sheets surrounding dipolarizing flux bundles in the magnetotail: The case for wedgelets. *Journal of Geophysical Research: Space Physics*, *118*, 2000–2020. https://doi.org/10.1002/jgra.50092

Liu, J., Angelopoulos, V., Zhou, X.-Z., & Runov, A. (2014). Magnetic flux transport by dipolarizing flux bundles. *Journal of Geophysical Research: Space Physics*, *119*, 909–926. https://doi.org/10.1002/2013JA019395

Liu, J., Angelopoulos, V., Zhou, X.-Z., Runov, A., & Yao, Z. (2013). On the role of pressure and flow perturbations around dipolarizing flux bundles. *Journal of Geophysical Research: Space Physics*, *118*, 7104–7118. https://doi.org/10.1002/2013JA019256

Liu, J., Angelopoulos, V., Zhou, X.-Z., Yao, Z.-H., & Runov, A. (2015). Cross-tail expansion of dipolarizing flux bundles. *Journal of Geophysical Research: Space Physics*, *120*, 2516–2530. https://doi.org/10.1002/2015JA020997

Liu, J., Lyons, L. R., Archer, W. E., Gallardo-Lacourt, B., Nishimura, Y., Zou, Y., et al. (2018). Flow shears at the poleward boundary of omega bands observed during conjunctions of swarm and THEMIS ASI. *Geophysical Research Letters*, *45*(3), 1218–1227. https://doi.org/10.1002/2017gl076485

Liu, J., Lyons, L. R., Wang, C. P., Hairston, M. R., Zhang, Y., & Zou, Y. (2020). Dawnside Auroral Polarization Streams. *Journal of Geophysical Research: Space Physics*, *125*. https://doi.org/10.1029/2019JA027742

Lühr, H., Park, J., Gjerloev, J. W., Rauberg, J., Michaelis, I., Merayo, J. M. G., & Brauer, P. (2015). Field-aligned currents' scale analysis performed with the Swarm constellation. *Geophysical Research Letters*, *42*(1), 1–8. https://doi.org/10.1002/2014GL062453

Lühr, H., Warnecke, J. F., & Rother, M. K. A. (1996). An algorithm for estimating field-aligned currents from single spacecraft magnetic field measurements: A diagnostic tool applied to Freja satellite data. *IEEE Transactions on Geoscience and Remote Sensing*, *34*(6), 1369–1376. https://doi.org/10.1109/36.544560

Lui, A. T. Y., Venkatesan, D., Anger, C. D., Akasofu, S.-I., Heikkila, W. J., Winningham, J. D., & Burrows, J. R. (1977). Simultaneous observations of particle precipitations and auroral emissions by the Isis 2 satellite in the 19-24 MLT sector. *Journal of Geophysical Research*, *82*(16), 2210–2226. https://doi.org/10.1029/JA082i016p02210

Lyons, L. R. (1981). Discrete aurora as the direct result of an inferred high-altitude generating potential distribution. *Journal of Geophysical Research*, *86*(A1), 1. https://doi.org/10.1029/JA086iA01p00001

Lyons, L. R., Nishimura, Y., Gallardo-Lacourt, B., Nicolls, M. J., Chen, S., Hampton, D. L., et al. (2015). Azimuthal flow bursts in the inner plasma sheet and possible connection with SAPS and plasma sheet earthward flow bursts. *Journal of Geophysical Research: Space Physics*, *120*(6), 5009–5021. https://doi.org/10.1002/2015ja021023

Lyons, L. R., Nishimura, Y., Xing, X., Runov, A., Angelopoulos, V., Donovan, E., & Kikuchi, T. (2012). Coupling of dipolarization front flow bursts to substorm expansion phase phenomena within the magnetosphere and ionosphere. *Journal of Geophysical Research*, *117*, 2212. https://doi.org/10.1029/2011JA017265

McDiarmid, I. B., Burrows, J. R., & Wilson, M. D. (1979). Large-scale magnetic field perturbations and particle measurements at 1400 km on the dayside. *Journal of Geophysical Research*, *84*(A4), 1431. https://doi.org/10.1029/JA084iA04p01431

McGranaghan, R. M., Mannucci, A. J., & Forsyth, C. (2017). A comprehensive analysis of multiscale field-aligned currents: Characteristics, controlling parameters, and relationships. *Journal of Geophysical Research: Space Physics*, *122*(12), 11–931. https://doi.org/10.1002/2017JA024742

McPherron, R. L., & Chu, X. (2016). Relation of the auroral substorm to the substorm current wedge. *Geoscience Letters*, *3*(1), 12. https://doi.org/10.1186/s40562-016-0044-5

McPherron, R. L., Russell, C. T., & Aubry, M. P. (1973). Satellite studies of magnetospheric substorms on August 15, 1968: 9. Phenomenological model for substorms. *Journal of Geophysical Research*, *78*, 3131–3149. https://doi.org/10.1029/JA078i016p03131

Mende, S. B., Harris, S. E., Frey, H. U., Angelopoulos, V., Russell, C. T., Donovan, E., et al. (2008). The THEMIS array of ground-based observatories for the study of auroral substorms. *Space Science Reviews*, *141*, 357–387. https://doi.org/10.1007/s11214-008-9380-x

Merayo, J. M. G., Jørgensen, J. L., Friis-Christensen, E., Brauer, P., Primdahl, F., Jørgensen, P. S., et al. (2008). *Small satellites for Earth observation* (pp. 143–151). Springer.

Merkin, V. G., Panov, E. V., Sorathia, K. A., & Ukhorskiy, A. Y. (2019). Contribution of bursty bulk flows to the global dipolarization of the magnetotail during an isolated substorm. *Journal of Geophysical Research: Space Physics*, *124*(11), 8647–8668. https://doi.org/10.1029/2019JA026872

Nakamura, R., Baumjohann, W., Schödel, R., Brittnacher, M., Sergeev, V. A., Kubyshkina, M., et al. (2001). Earthward flow bursts, auroral streamers, and small expansions. *Journal of Geophysical Research*, *106*, 10791–10802. https://doi.org/10.1029/2000JA000306

Nishida, A. (1979). Possible origin of transient dusk-to-dawn electric field in the nightside magnetosphere. *Journal of Geophysical Research*, *84*(A7), 3409. https://doi.org/10.1029/JA084iA07p03409

Nishimura, Y., Lyons, L. R., Gabrielse, C., Weygand, J. M., Donovan, E. F., & Angelopoulos, V. (2020). Relative contributions of large-scale and wedgelet currents in the substorm current wedge. *Earth Planets and Space*, *72*(1), 106. https://doi.org/10.1186/s40623-020-01234-x

Nishimura, Y., Yang, J., Pritchett, P. L., Coroniti, F. V., Donovan, E. F., Lyons, L. R., et al. (2016). Statistical properties of substorm auroral onset beads/rays. *Journal of Geophysical Research: Space Physics*, *121*(9), 8661–8676. https://doi.org/10.1002/2016ja022801

Ohtani, S., & Gjerloev, J. W. (2020). Is the substorm current wedge an ensemble of wedgelets?: Revisit to midlatitude positive bays. *Journal of Geophysical Research: Space Physics*, *125*(9). https://doi.org/10.1029/2020JA027902

Ohtani, S., Kokubun, S., Elphic, R. C., & Russell, C. T. (1988). Field-aligned current signatures in the near-tail region: 1. ISEE observations in the plasma sheet boundary layer. *Journal of Geophysical Research*, *93*(A9), 9709. https://doi.org/10.1029/JA093iA09p09709

Ohtani, S., Wing, S., Newell, P. T., & Higuchi, T. (2010). Locations of night-side precipitation boundaries relative to R2 and R1 currents. *Journal of Geophysical Research*, *115*(A10). https://doi.org/10.1029/2010ja015444

Paxton, L. J., Schaefer, R. K., Zhang, Y., Kil, H., & Hicks, J. E. (2018). SSUSI and SSUSI-lite: Providing space situational awareness and support for over 25 years. *Johns Hopkins APL Technical Digest*, *34*(3).

Pearson, K. (1901). LIII. On lines and planes of closest fit to systems of points in space. *The London, Edinburgh, and Dublin Philosophical Magazine and Journal of Science*, *2*(11), 559–572. https://doi.org/10.1080/14786440109462720

Rich, F. J. (1984). *Fluxgate magnetometer (SSM) for the Defense Meteorological Satellite Program (DMSP) Block 5D-2, flight 7*. Tech. Rep. AFGL-TR-84-0225, Air Force Geophys. Lab., Hanscom Air Force Base, Mass.

Rich, F. J., & Hairston, M. (1994). Large-scale convection patterns observed by DMSP. *Journal of Geophysical Research*, *99*(A3), 3827. https://doi.org/10.1029/93JA03296

Ritter, P., & Lühr, H. (2008). Near-Earth magnetic signature of magnetospheric substorms and an improved substorm current model. *Annales Geophysicae*, *26*, 2781–2793. https://doi.org/10.5194/angeo-26-2781-2008

Saflekos, N. A., Sheehan, R. E., & Carovillano, R. L. (1982). Global nature of field-aligned currents and their relation to auroral phenomena. *Reviews of Geophysics*, *20*(3), 709. https://doi.org/10.1029/RG020i003p00709

Sergeev, V. A., Angelopoulos, V., Gosling, J. T., Cattell, C. A., & Russell, C. T. (1996). Detection of localized, plasma-depleted flux tubes or bubbles in the midtail plasma sheet. *Journal of Geophysical Research*, *101*(A5), 10817–10826. https://doi.org/10.1029/96ja00460

Sergeev, V. A., Liou, K., Newell, P. T., Ohtani, S.-I., Hairston, M. R., & Rich, F. (2004). Auroral streamers: Characteristics of associated precipitation, convection and field-aligned currents. *Annales Geophysicae*, *22*(2), 537–548. https://doi.org/10.5194/angeo-22-537-2004

Sergeev, V. A., Tsyganenko, N. A., Smirnov, M. V., Nikolaev, A. V., Singer, H. J., & Baumjohann, W. (2011). Magnetic effects of the substorm current wedge in a "spread-out wire" model and their comparison with ground, geosynchronous, and tail lobe data. *Journal of Geophysical Research*, *116*. https://doi.org/10.1029/2011JA016471

Strangeway, R. J. (2012). *The relationship between magnetospheric processes and auroral field-aligned current morphology*. In K. Andreas, E. Donovan, F. Bagenal, & T. Karlsson (Eds.), Geophysical Monograph series (pp. 355–364). American Geophysical Union. https://doi.org/10.1029/2012GM001211

Sugiura, M., Maynard, N. C., Farthing, W. H., Heppner, J. P., Ledley, B. G., & Cahill, L. J. (1982). Initial results on the correlation between the magnetic and electric fields observed from the DE-2 satellite in the field-aligned current regions. *Geophysical Research Letters*, *9*(9), 985–988. https://doi.org/10.1029/GL009i009p00985

Sun, W. J., Fu, S. Y., Parks, G. K., Liu, J., Yao, Z. H., Shi, Q. Q., et al. (2013). Field-aligned currents associated with dipolarization fronts. *Geophysical Research Letters*, *40*, 4503–4508. https://doi.org/10.1002/grl.50902

Tanaka, T. (1995). Generation mechanisms for magnetosphere-ionosphere current systems deduced from a three-dimensional MHD simulation of the solar wind-magnetosphere-ionosphere coupling processes. *Journal of Geophysical Research*, *100*(A7), 12057. https://doi.org/10.1029/95ja00419

Vasyliunas, V. M. (1970). Mathematical Models of Magnetospheric Convection and Its Coupling to the Ionosphere. *Particles and Field in the Magnetosphere*, *17*, 60–71. https://doi.org/10.1007/978-94-010-3284-1_6

Vickrey, J. F., Livingston, R. C., Walker, N. B., Potemra, T. A., Heelis, R. A., Kelley, M. C., & Rich, F. J. (1986). On the current-voltage relationship of the magnetospheric generator at intermediate spatial scales. *Geophysical Research Letters*, *13*(6), 495–498. https://doi.org/10.1029/GL013i006p00495

Wang, C.-P., Gkioulidou, M., Lyons, L. R., & Wolf, R. A. (2018). Spatial distribution of plasma sheet entropy reduction caused by a plasma bubble: Rice convection model simulations. *Journal of Geophysical Research: Space Physics*, *123*(5), 3380–3397. https://doi.org/10.1029/2018ja025347

Wang, C.-P., Lyons, L. R., Wolf, R. A.., Nagai, T., Weygand, J. M., & Lui, A. T. Y. (2009). Plasma sheet P5/3 and n and associated plasma and energy transport for different convection strengths and AE levels. *Journal of Geophysical Research*, *114*(A9), https://doi.org/10.1029/2008JA013849

Wang, C.-P., Xing, X., Liu, Y.-H., & Runov, A. (2018). A case study of connection between ground magnetic field perturbations and tail current sheet bursty flows at X = −60 R E. *Journal of Geophysical Research: Space Physics*, *123*(3), 1822–1833. https://doi.org/10.1002/2017JA024972

Wang, C.-P., Yang, J., Gkioulidou, M., Lyons, L. R., & Wolf, R. A. (2020). Generation and evolution of two opposite types of mesoscale plasma sheet bubbles. *Journal of Geophysical Research: Space Physics*, *125*(9). https://doi.org/10.1029/2020JA028072

Wang, Z., Zou, S., Coppeans, T., Ren, J., Ridley, A., & Gombosi, T. (2019). Segmentation of SED by boundary flows associated with westward drifting partial ring current. *Geophysical Research Letters*, *46*(14), 7920–7928. https://doi.org/10.1029/2019GL084041

Xing, X., Lyons, L. R., Nishimura, Y., Angelopoulos, V., Donovan, E., Spanswick, E., et al. (2011). Near-Earth plasma sheet azimuthal pressure gradient and associated auroral development soon before substorm onset. *Journal of Geophysical Research*, *116*. https://doi.org/10.1029/2011JA016539

Yang, J., Toffoletto, F. R., & Song, Y. (2010). Role of depleted flux tubes in steady magnetospheric convection: Results of RCM-E simulations. *Journal of Geophysical Research*, *115*(A5). https://doi.org/10.1029/2010JA015731

Yang, J., Toffoletto, F. R., & Wolf, R. A. (2014). RCM-E simulation of a thin arc preceded by a north-south-aligned auroral streamer. *Geophysical Research Letters*, *41*, 2695–2701. https://doi.org/10.1002/2014GL059840

Yang, J., Toffoletto, F. R., Wolf, R. A., Sazykin, S., Ontiveros, P. A., & Weygand, J. M. (2012). Large-scale current systems and ground magnetic disturbance during deep substorm injections. *Journal of Geophysical Research*, *117*. https://doi.org/10.1029/2011JA017415

Yao, Z. H., Pu, Z. Y., Fu, S. Y., Angelopoulos, V., Kubyshkina, M., Xing, X., et al. (2012). Mechanism of substorm current wedge formation: THEMIS observations. *Geophysical Research Letters*, *39*, 13102. https://doi.org/10.1029/2012GL052055

Yue, C., Wang, C. P., Nishimura, Y., Murphy, K. R., Xing, X., Lyons, L., et al. (2015). Empirical modeling of 3-D force-balanced plasma and magnetic field structures during substorm growth phase. *Journal of Geophysical Research: Space Physics*, *120*(8), 6496–6513. https://doi.org/10.1002/2015JA021226